

To Dr. Roussos, Topical Editor

The submitted manuscript has been substantially revised by including new calculations of slow magnetoacoustic wave with detailed explanation of field and particle measurements by satellite in multiple Pi2 event. A new section was added to explain why we use very low latitude Pi2s to time the onset of field line dipolarization.

Each issue has been addressed in the prescribed Comment/Response format. These responses were highlighted in bold typeface. Due to the addition of new sections and new calculations in Appendix, the introduction and related paragraphs were revised. They are also shown in boldface.

Point-by-point replies to the comments raised by Referee #3 is given below.

**Comment 1.**

1. The paper is too much detached from the discussed observations. Numerous parts of the paper refer to spacecraft data and figures that were presented in earlier publications of the author. I believe that a research paper should not depend heavily on another paper. On the contrary, most of the data that is discussed in the present paper, should also be readily available for readers in the paper's figures. Of course, the figures may not be just copied from a previous research. Instead, they should be prepared for the purposes of the present paper.

**Response**

The field line dipolarization is explained in this paper as a relaxation process by scattering the radial inhomogeneity to the dawn-dusk directions. The main point is what caused initial buildup of the radial inhomogeneity and the triggering mechanisms which relaxed these inhomogeneities in the magnetotail. We proposed in this paper that slow magnetoacoustic wave initiated by Ballooning instability relaxed the radial inhomogeneities accumulated in the pre-onset intervals by the inflows.

We provided an example of relaxation processes of radial inhomogeneities from satellite observations. Also, we developed a theoretical model of slow magnetoacoustic wave for producing anisotropic flux distributions in pitch angle spectrogram that may lead to a scattering of the radial inhomogeneities and resulted field line dipolarization.

In this revision, we discussed the observed field line dipolarization in the refined theoretical model.

## **Comment 2.**

2. The author supports the presented idea by some criteria estimates rather than by real observations. For example, the author derives the threshold for the ballooning instability and claims that the condition is fulfilled. On the other hand, there is no observational figure showing signatures of the ongoing instability development.

Not being aware of whether the ballooning instability was excited, the author further suggests that the instability drives a slow wave (the next event in the author's scenario). Here again, there are neither provided observational evidences of the presence of the slow wave, nor theoretical details are explained how the ballooning instability generates such a slow mode wave. If such details can be found in another paper, then a short summary on the process would be reasonable to include in the present paper. By the way, it may be better to give a reference to Kadomtsev in English rather than in Japanese or Russian.

A similar situation concerns the next steps in the author's scenario – azimuthal spreading of plasmas, decrease of the radial pressure gradient, reduction of the cross-tail currents and pileup of the magnetic field.

Thus, the paper could be more supported by specific observations (perhaps by a new event with many spacecraft). An alternative way to improve the paper would be developing a more complete and consistent theoretical model. Unfortunately, at this stage the paper looks like a presentation of a concept rather than a rigorous theoretical or observational analysis.

## **Response**

Please refer to our response to Comment 1.

Kadomtsev [1976] was published only in Russian and Japanese. We presented a theoretical model of dipolarization using slow magnetoacoustic wave and its application to the pitch angle spectrogram. These are found in Appendix and in Section 4 (Excitation of slow magnetoacoustic wave). In the new section 5.1 (Relaxation of radial inhomogeneity), satellite observations relating to the relaxation of radial inhomogeneities are presented to complement the theoretical work of slow magnetoacoustic wave.

### Comment 3.

3. Another major concern is that the paper does not provide adequate literature research on the paper's main topic (inner magnetosphere and magnetotail dipolarization and dipolarization fronts).

For example, from VAP and earlier observations it is known that dipolarization fronts may reach geostationary and deeper altitudes (down to L=4):

Moore, T. E., et al., (1981). Propagating substorm injection fronts. *Journal of Geophysical Research*, 86, 6713–6726. <https://doi.org/10.1029/JA086iA08p06713>

Reeves, G. D., et al., . (1990). Multi-satellite measurements of the substorm injection region. *Geophysical Research Letters*, 17, 2015–2018. <https://doi.org/10.1029/GL017i011p02015>

Ohtani, S., et al., (2018). Spatial development of the dipolarization region in the inner magnetosphere. *Journal of Geophysical Research: Space Physics*, 123, 5452–5463. <https://doi.org/10.1029/2018JA025443>.

Conditions that define the penetration depth were experimentally discussed, e.g., in

Dubyagin, S., et al., (2011). Can flow bursts penetrate into the inner magnetosphere? *Geophysical Research Letters*, 38, L08102. <https://doi.org/10.1029/2011GL047016>

An global modeling analysis of dipolarization was made recently in

Merkin, V. G., et al., (2019). Contribution of bursty bulk flows to the global dipolarization of the magnetotail during an isolated substorm. *Journal of Geophysical Research: Space Physics*, 124. <https://doi.org/10.1029/2019JA026872>

The authors may want to go through reference lists in the above papers in order to construct a more appropriate literature analysis in the present paper.

### **Response**

Electric field drifts associated with convection surge match earthward transport velocity (10 - 100 km/s) of injection front at geosynchronous orbit [Moore et al., 1981] as well as dawn-

dusk propagation velocity (30 km/s) of the dipolarization region [Saka and Hayashi, 2017]. This expansion velocity in longitudes is equal to the curvature/gradient drift of 30 keV particles at geosynchronous orbit, suggesting that higher energy particles than 30 keV escape from the injection region. Trajectories of high energy particles above 100 keV can be used to trace back the initial onset region by the satellite constellation along the geosynchronous orbit [Reeves et al., 1990]. Possible conjunctions between dipolarization region and injection region will be studied elsewhere in future.

We referred to Ohtani et al., [2018] in the text [Lines 241-250] suggesting that “..... most of the flux tube transition may occur tailward of geosynchronous orbit. Some of the events, however, may happen earthward of the geosynchronous orbit [i.e., Ohtani et al., 2018]”.

An arrival of low entropy plasma bubbles into the inner magnetosphere [e.g., Dubyagin et al., 2011] may breakdown the last open trajectories of plasma sheet electrons. This may cause N-S auroras from poleward aurora boundary [Saka et al., JASTP, 145, 114-124, 2016], However, if enough field line stretching was developed in the midnight magnetosphere prior to the arrival of the bubble, the plasma bubble may trigger auroras arising out of arc (substorm onset). The latter case may not be inconsistent with the global dipolarization model of inner magnetosphere [Merkin et al., 2019] where intensity and occurrence of dipolarization front (DF) may increase abruptly at substorm onset. These topics will be the subject of future study.

Comment 4.

4. The author relies on Pi2 pulsations onset time at various ground stations. If I understand correctly, the onset of Pi2 pulsations is needed for timing of the dipolarization. It is not explained though how the Pi2 pulsations fit in the author’s model. As it follows from some models, Pi2 pulsations can occur independently from dipolarization (<https://doi.org/10.1002/2014JA020625>) Also, it has been suggested that low latitude Pi2 pulsations are directly driven by compressional pulses <https://doi.org/10.1029/2000JA000158> . High-latitude Pi2 pulsations were suggested to be driven by magnetospheric buoyancy waves <https://doi.org/10.1002/2013JA019633>.

## **Response**

Generation model of Pi2 pulsations that fits our scenario is presented in new Section 7.

This model includes the “directly driven” model of [Kepko et al., JGR, 2001] and the

“magnetospheric buoyancy wave” model of [Panov et al., 2014] because periodic arrival of BBF substructure, or DF, yielded periodic oscillations of negative bay (or equivalently dipolarization). Also “impinging on inner magnetosphere from plasma sheet” [Lysak et al., 2014] is analogous to excitation of cavity mode in low latitudes by the periodic compressions produced by oscillating positive bay.

1 The increase of curvature radius of geomagnetic field lines preceding a classical  
2 dipolarization

3  
4  
5 Osuke Saka

6 Office Geophysik, Ogoori, 838-0141, Japan  
7  
8

9 Abstract

10 **Based on assumptions that substorm field line dipolarization at geosynchronous**  
11 **altitudes is associated with the arrival of high velocity magnetotail flow bursts referred**  
12 **to as Bursty Bulk Flows, we propose following sequence of field line dipolarization:**  
13 **(1) Slow magnetoacoustic wave excited through Ballooning instability by enhanced**  
14 **inflows in pre-onset intervals towards the equatorial plane; (2) In the equatorial plane,**  
15 **slow magnetoacoustic wave stretching of the flux tube in dawn-dusk directions**  
16 **resulting in spreading plasmas in dawn-dusk directions and reduction in the radial**  
17 **pressure gradient in the flux tube. As a consequence of the foregoing processes, the**  
18 **flux tube assumes a new equilibrium geometry in which curvature radius of new field**  
19 **lines increased in the meridian plane suggesting an onset of field line dipolarization.**  
20 **The dipolarization processes associated with changing the curvature radius preceded**  
21 **classical dipolarization caused by reduction of cross-tail currents and pileup of the**  
22 **magnetic fields.**

23 **Increasing curvature radius induced convection surge in the equatorial plane as well**  
24 **as inductive westward electric fields of the order of mV/m. Electric fields transmitted**  
25 **to the ionosphere produce electromotive force in the E layer for generating field-**  
26 **aligned current system of Bostrom type. This is also equivalent to the creation of an**  
27 **incomplete Cowling channel in the ionospheric E layer by the convection surge.**  
28  
29

### 30 **1. Introduction**

31 Substorms are spatially localized and temporarily variable processes in the nighttime  
32 magnetosphere. It is often difficult to determine onset timing of substorm processes such as  
33 magnetotail flow burst, field line dipolarization, and particle injections. To resolve the timing  
34 uncertainties, auroras in global satellite images [Nakamura et al., 2001; Miyashita et al.,  
35 2009], intensifications of auroral kilometric radiation [Fairfield et al., 1999; Morioka et al.,  
36 2010], and dispersionless particle injection in geosynchronous orbit [Birn et al., 1997] were

37 used. Ground Pi2 pulsations are another useful tool for determination of the substorm timing  
38 [Sakurai and Saito, 1976; Nagai et al., 1998; Baumjohann et al., 1999]. Particularly, Pi2s in  
39 equatorial region exhibited small phase difference ( $m < 1$ ,  $m$  denotes azimuthal wave number)  
40 across widely separated stations in the equatorial countries [Kitamura et al., 1988],  
41 minimizing the timing uncertainties arising from delays in longitudinal propagations. This  
42 enabled us accurate onset timing study of substorms using magnetometer data from two  
43 remote locations, geosynchronous altitudes and ground stations of the equatorial countries  
44 [Saka et al., 2010].

45 In this study, we focus on the dipolarization events at geosynchronous orbit from growth to  
46 expansion phase. Triggering mechanisms of the field line dipolarization in the vicinity of  
47 geosynchronous orbit are our major concern. In this paper, onset timing study of substorms  
48 using magnetometer data from equatorial countries are summarized in Sect. 2. In Sect. 3,  
49 we present a pre-onset scenario leading to the dipolarization onset. In Sect. 4, excitation of  
50 slow magnetoacoustic wave is discussed for triggering field line depolarization. We will focus  
51 on the field line dipolarization in the vicinity of geosynchronous orbit in Sect. 5. A coupling of  
52 magnetosphere and ionosphere associated with this dipolarization scenario will be presented  
53 in Sect. 6. **In Sect. 7, we present a triggering mechanism of low latitude Pi2s that**  
54 **enabled the Pi2-based epoch analyses.** Summary and discussion of this scenario is given  
55 in Sect. 8.

56  
57

## 58 **2. Summary of onset timing study using ground Pi2s at the equator**

59 In this section, we summarize field line dipolarization occurring at the geosynchronous orbit  
60 based on the statistical results obtained by Saka et al. [2010]. The authors used  
61 magnetometer data from geosynchronous satellites (Goes5 and Goes6) and those at ground  
62 equatorial stations (Huancayo, Peru,  $1.4^\circ N$  in geomagnetic latitudes) in the conjugate  
63 meridian. Goes5 was located at higher latitudes,  $10.3^\circ N$  in dipole coordinates, and Goes6  
64 was closer to the equator;  $7.9^\circ N$  in dipole coordinates. This difference was caused by the  
65 separated meridians of the satellites (2.2 hours of local time). The dipole coordinate used are  
66 equivalent to the HDV coordinates; H is positive northward along the dipole axis, V is radial  
67 outward, and D denotes dipole east. The field line dipolarization at the geosynchronous orbit  
68 can be characterized either by a step-like or impulsive increase of inclination angle of the  
69 geomagnetic field lines. The inclination angle is measured positive northward from the dipole  
70 equator. The step-like dipolarization was observed by Goes5 located at higher latitudes, while  
71 the dipolarization pulse was observed by Goes6 at latitudes closer to the equatorial plane.  
72 The onset of field line dipolarization preceded the initial peak of the ground Pi2 pulse by two

73 minutes, suggesting that the onset was initiated in association with the first increase of the  
74 Pi2 amplitudes. **Following the dipolarization onset, field line magnitude decreased at**  
75 **the geosynchronous orbit, and field lines deflected westward in the dawn sector and**  
76 **eastward in the dusk sector (see Figure 1 for dawn-dusk deflection, reproduced from**  
77 **[Saka et al., 2010]). This is caused by the dawn-dusk expansion of the plasma flows**  
78 **occurring tailward of the geosynchronous orbit. These longitudinal expansions lasted**  
79 **for about 10 min and decreased the field magnitudes therein. Expansion in the dusk**  
80 **sector, however, continued over this characteristic 10-min-interval. Asymmetries of**  
81 **the dawn-dusk expansion may be caused by diamagnetic drifts in the plasma sheet**  
82 **[Liu et al., 2013].** It is suggested that classical dipolarization, caused by the reduction of  
83 cross-tail currents in the midnight magnetosphere, happened after the nightside  
84 magnetosphere experienced this characteristic 10-min-interval. For this reason, the first 10  
85 min intervals are referred to as transitional state of substorm expansion [Saka et al., 2010].  
86  
87

### 88 **3. Pre-onset intervals leading to field line dipolarization**

89 In the pre-onset intervals, decrease of the field line inclination started two hours prior to the  
90 dipolarization onset. It attained minimum angles ( $33.6^\circ$  for Goes5 and  $49.4^\circ$  for Goes6 in  
91 dipole coordinates) right before the dipolarization onset [Saka, 2010; 2019].

92 One of the properties of plasmas in pre-onset intervals are continuing inflows of lobe plasmas  
93 towards the equatorial plane [Birn and Hesse, 1996], Poynting flux enhancement [Machida  
94 et al., 2009], and  $E_y$  (westward electric fields) penetration toward the equatorial plane  
95 [Machida et al, 2014]. Corresponding plasma properties at geosynchronous altitudes may be  
96 predominant perpendicular temperature anisotropies of thermal plasmas (30eV - 40keV)  
97 obtained from three-dimensional temperature matrix and their gradual decrease towards the  
98 onset [Birn et al., 1997]. At the onset, however, increase of parallel anisotropy stopped and  
99 perpendicular anisotropy increased again. Such changes of temperature anisotropy at onset  
100 were observed in roll-angle spectrogram of energy flux of electrons in 15eV-40keV [Saka and  
101 Hayashi, 2017]. This transition of the temperature anisotropies may be accounted for by the  
102 following scenario.

103 **A continuing tailward stretch of the field lines in the pre-onset intervals as depicted in**  
104 **Figure 2 may increase equatorward flux by the counterclockwise rotation of the inflow**  
105 **vectors ( $F_{\perp}$ ) in the north of the equatorial plane (clockwise rotation in the south) and**  
106 **produce a parallel component as well by the relation,**



107 
$$\delta F_{\parallel} = F_{\perp} (\omega \cdot \delta t) \quad (1)$$

108 Here,  $\delta F_{\parallel}$  denotes increase of parallel flux per time,  $\delta t$ ,  $\omega$  is angular velocity of rotation  
 109 of  $F_{\perp}$  vectors associated with the thinning of the flux tubes caused by stretching. In pre-  
 110 onset intervals lasting 90 min at geosynchronous altitudes, field line stretching decreased the  
 111 field line inclination by  $7^{\circ}$  from  $40.6^{\circ}$  to  $33.6^{\circ}$  [Saka, 2019]. This gives angular velocity  
 112 of rotation of field line inclination in equation (1) as  $1.4 \times 10^{-3} \text{ rad} / \text{min}$ . Total parallel flux  
 113 gained in T min may be given by the integral of equation (1) with time from 0 to T. Substituting  
 114 T=60 min and  $1.4 \times 10^{-3} \text{ rad} / \text{min}$  for angular velocity of field line inclination, this yields  
 115  $F_{\parallel} = 8.2 \times 10^{-2} \cdot F_{\perp}$ . Gain of  $F_{\parallel}$  is about 10% of the perpendicular flux ( $F_{\perp}$ ). This is  
 116 consistent with the parallel temperature anisotropies gained prior to the onset (20% gain) in  
 117 geosynchronous orbit [Birn et al., 1997].

118 Continuing parallel flux flows associated with the flux tube stretching in the pre-onset intervals  
 119 may increase plasma pressures in the flux tube at its tailward end. This condition leads to  
 120 further stretching of the flux tube (small curvature radius) [Ohtani and Tamao, 1993; Rubtsov  
 121 et al., 2018] by the relation,

122 
$$\frac{\beta}{2} \kappa + \kappa_B + \frac{1}{R} = 0 \quad (2)$$

123 Here,  $\beta$  is plasma to magnetic pressure ratio,  $\kappa$  and  $\kappa_B$  denote reciprocal spatial scales  
 124 of radial inhomogeneity of plasma pressure and magnetic fields in the equatorial plane,  
 125 respectively. R is curvature radius of the field lines.

126  
 127

#### 128 **4. Excitation of slow magnetoacoustic wave**

129 The continuing parallel flows may excite magnetoacoustic wave. From a set of linearized  
 130 MHD equations we have relation between parallel displacement along the field lines ( $\xi_z$ )  
 131 and divergence of perpendicular displacements ( $\xi_{\perp}$ ) in the following form (see Appendix),

132 
$$\xi_z = \frac{C_s^2}{\omega^2} F \cdot B_0^2 \frac{\partial}{\partial z} (\text{div} \xi_{\perp}) \quad (3)$$

133 Here,  $C_s$ ,  $\omega$  and  $B_0$  are the sound velocity, angular frequency of waves and background  
 134 field magnitudes, respectively.  $F$  is given by

$$135 \quad F = \frac{C_A^2}{B_0^2} \frac{1}{C_s^2 - \left(\frac{\omega}{k}\right)^2} \quad (4)$$

136  $F$  is positive for the slow magnetoacoustic wave and negative for the fast magnetoacoustic  
 137 wave.  $C_A$  and  $k$  denote Alfvén velocity and wave vector, respectively. **We use equation (3)**  
 138 **for the classification of slow and fast magnetoacoustic waves. Slow magnetoacoustic**  
 139 **wave yields perpendicular expansion of the flux tubes at the converging point of**  
 140 **parallel flows on the equatorial plane. For fast wave, perpendicular shrinkage of flux**  
 141 **tubes occurs at the converging point of parallel flows (equatorial plane).**

142 **The equation (3) will be applied to simulate possible effect of magnetoacoustic wave**  
 143 **on pitch angle spectrogram. For this, we used drift Maxwell distributions for phase**  
 144 **space density (PSD) assuming gyrotropy for particle trajectories. PSD was composed**  
 145 **of three parts: one drifting parallel, another anti-parallel along the field lines, and the**  
 146 **third part perpendicular to the field lines. Figure 3(A) shows pitch angle spectrogram**  
 147 **of energy flux with no drift velocities either perpendicular or parallel to the background**

148 **field lines. Energy flux is defined by  $(2E^2/m^2)f$ , where  $E$ ,  $m$ ,  $f$  are energy, mass of**  
 149 **particles, and phase space density, respectively. Energy flux is given in**  
 150  **$eV / (cm^2 s \cdot sr \cdot eV)$ . Only parallel drift increased in from  $0.3V_{th}$ ,  $0.6V_{th}$ , and to  $1.0V_{th}$  as**  
 151 **shown in B, C, and D. For E and F, perpendicular drift increased to  $0.3V_{th}$  and  $0.5V_{th}$**   
 152 **while parallel drift remained at  $1.0V_{th}$ . Energy fluxes initially in quasi tapped**  
 153 **distribution (A) changed to more parallel and anti-parallel fluxes as parallel and anti-**  
 154 **parallel drift increased (B, C, and D). Increasing perpendicular drifts increased**  
 155 **perpendicular fluxes in the pitch angle distributions of E and F.**

156 **We clarified that magnetoacoustic wave produced coupling of parallel flux along the**  
 157 **field lines and the perpendicular flux. However, we choose slow magnetoacoustic**  
 158 **wave for the wave mode because the flux tubes expanded (did not shrink) in the**  
 159 **transitional interval as discussed in Section 2. Slow magnetoacoustic wave may be**  
 160 **triggered through Ballooning instability, when enough pressure gradient is**  
 161 **accomplished in an earthward direction [Ohtani and Tamao, 1989; Rubtsov et al., 2018].**

162 We can estimate the Ballooning instability threshold  $\kappa$  (reciprocal scale of radial  
 163 inhomogeneity of plasma pressure) using calculation results given in [Rubtsov et al., 2018].

164 In a distance from  $L=5$  to  $10R_e$ , instability threshold is given approximately as  $\kappa = -1.0R_e^{-1}$   
 165 ( $\kappa$  denotes reciprocal spatial scale of radial inhomogeneity of plasma pressure, and  $R_e$  is

166 the Earth radius) for beta defined by the ratio of plasma pressure and magnetic pressure  
167 exceeding 0.1. This suggests that the Ballooning instability develops at the geosynchronous  
168 altitudes (curvature radius  $R$  is 2.2  $R_E$ ) when spatial scale of the earthward pressure gradient  
169 caused by the inflows becomes steeper than 1.0  $R_E$ . We show in the following section that  
170 this theoretical consideration matched observations.

171

172

## 173 **5. Field line dipolarization in the vicinity of geosynchronous orbit**

### 174 **5.1 Relaxation of radial inhomogeneity**

175 We can assume the westward electric fields in Dipolarization Front (DF) [Runov et al., 2011]  
176 embedded in the leading edge of Bursty Bulk Flow (BBF) as external stimulus for triggering  
177 Ballooning instability. In this case westward electric fields in the DF temporarily amplified the  
178 parallel flux flowing towards the end point of the flux tube in the equatorial plane and further  
179 steepen earthward pressure gradient. If it exceeds instability threshold determined by  $\beta$   
180 and initial curvature radius  $R$ , slow magnetoacoustic wave can be excited [Rubtsov et al.,  
181 2018]. Once the slow magnetoacoustic wave was excited, perpendicular fluxes spread the  
182 plasmas in dawn-dusk directions and smooth (or relax) the radial gradient of plasma  
183 pressures in the equatorial plane (smaller  $\kappa$ ). This may result in the transition of the flux  
184 tube geometry to a new configuration, an increase of the curvature radius of the field lines  
185 (larger  $R$ ) (see equation (2)).

186 **We revisit multiple Pi2 events observed by AMPTE CCE on 31 August 1986 [Saka et**  
187 **al., 2002] and show an example of relaxation of radial inhomogeneity of plasma**  
188 **pressures associated with field line dipolarization in Figure 4. The satellite passed the**  
189 **midnight sector (20 – 23 MLT) from 3  $R_E$  to 7  $R_E$  at latitudes south of the equatorial**  
190 **plane ( $-8^\circ$  MLat) when multiple Pi2 event (with positive bay) were observed at low**  
191 **latitude station (KUJ) at  $L=1.2$  in the midnight sector (Figure 4A). Inclination angle of**  
192 **field lines along the satellite trajectory is shown in Figure 4(B). Dipolarization occurred**  
193 **as marked by vertical arrows correlating to multiple onset of Pi2s, 1 through 4 in Figure**

194 **4(A). Ion fluxes coming from dawn sector ( $J_-$ ) and from dusk sector ( $J_+$ ) at satellite**  
195 **altitudes were measured by the instruments (two energy channels, 63-85 keV and 125-**  
196 **210 keV) on board AMPTE CCE [Takahashi et al., 1996]. A schematic of particle**  
197 **measurement is shown at the top of Figure 5. The flux difference ( $J_- - J_+ > 0$ )**  
198 **increased in association with the onset of multiple Pi2 (15:05 UT) and positive bay at**  
199 **KUJ (Figures 4C and 4D). Sudden increase was followed by the slow decrease of flux**

200 in 63-85 keV channel and rapid decrease of flux in 125-210 keV channel. The flux  
 201 difference,  $J_- > J_+$ , may be caused either by earthward pressure gradient or  
 202 westward convection of plasmas. From the different patterns of the flux decrease with  
 203 time in two energy channels, we can suggest that the measured flux difference,  
 204  $J_- - J_+$ , can be attributed to increase of the earthward pressure gradient and  
 205 succeeding relaxation. Note that guiding center of  $J_- / J_+$  is earthward/tailward of the  
 206 satellite position as depicted in top of Figure 5. The different relaxation speed in two  
 207 energy channels, slower for 63-85 keV and faster for 125-210 keV, suggest that the  
 208 earthward pressure gradient (assumed to be proportional to the flux gradient)  
 209 decreased with time during the multiple Pi2 event (Figure 5). The flux difference (50  
 210 counts/sample) was 10% of the background flux both for 63-85 keV (Larmor radius is  
 211 250 km for 150 nT) and for 125-210 keV (Larmor radius is 450 km), that is, the flux level  
 212 differed by 10% at two locations 1000 km apart in radial distance for 63-85 keV and  
 213 1800 km for 125-210 keV. This gives e-folding scale of the earthward pressure gradient  
 214 being 0.98 Re and 1.77 Re for 63-85 keV and 125-210 keV, respectively. The 31 August  
 215 event shows that radial pressure gradient was relaxed in the inner magnetosphere in  
 216 association with the increase of the field line inclination (dipolarization). Although the  
 217 field line dipolarization showed a sharp onset in satellite magnetometer data, we note  
 218 that it did not occur in ion flux data. This may be true because the ion flux change at  
 219 the onset may be obscured by the contamination from the past onsets transported  
 220 across the field lines from the adjoining sector by the electric fields and  
 221 gradient/curvature drifts. We conclude that the relaxation of spatial inhomogeneity  
 222 started when the spatial scale of the radial inhomogeneity approached 1.0 Re,  
 223 consistent with theoretical consideration of Ballooning instability by Rubtsov et al  
 224 (2018).

225

## 226 **5.2 Flux tube transition to a new geometry**

227 Meanwhile, field lines in the further earthward locations may be compressed by the inward  
 228 movement of the outer field lines. This process associated with the dipolarization onset may  
 229 increase the parameter  $\kappa_B$  in equation (2) which may result in transition to a new geometry  
 230 of earthward field lines, a decrease of the curvature radius  $R$ . Transition of the field line  
 231 geometries for onset locations and ones in earthward locations are schematically illustrated  
 232 in Figure 6. These field line geometries in meridian plane matched the third harmonic and

233 fundamental harmonic deformations of outer and inner field lines, respectively. This is often  
234 observed in the midnight magnetosphere in the initial pulse of Pi2s [Saka et al., 2012].  
235 Transitions of the flux tube geometry in magnetosphere also correspond to the production of  
236 negative bay in higher latitudes and positive bay in lower latitudes. If we can assume that  
237 negative bay switched to positive bay at latitudes, 60 degrees in geomagnetic coordinates  
238 for examples, this latitude can be mapped beyond the geosynchronous orbit ( $L \sim 7 R_E$  or  
239 further tailward) as field line dipolarization occurs along the stretched flux tubes.  
240 Consequently, this scenario requires that the BBFs are not necessary to reach inner  
241 magnetosphere to trigger the substorm onset at lower latitudes. **In the inset, flux tube**  
242 **deformations are illustrated in the equatorial cross section at onset locations (field**  
243 **lines 1 and 2). Divergence of perpendicular flows (solid arrows) produced dawn-dusk**  
244 **expansion of flux tube (2) and the shrinkage of stretched flux tube (1) by relaxation of**  
245 **the radial inhomogeneity. Flux tube deformation from 1 to 2 tended to preserve the**  
246 **total magnetic fluxes in the equatorial cross section. From the local time distribution**  
247 **of the dawn-dusk expansion of the flux tubes shown in Figure 1, most of the flux tube**  
248 **transition such as from 1 to 2 may occur tailward of geosynchronous orbit. Some of**  
249 **the events, however, may happen earthward of the geosynchronous orbit [i.e., Ohtani**  
250 **et al., 2018].**

251 Increasing of the curvature radius, or earthward shrinkage of the flux tubes, produce a  
252 reduction of the radial component of the field lines ( $V$  in dipole coordinates) by adding positive  
253  $V$  in the north of the equatorial plane and negative  $V$  in the south. If amplitudes of the  $V$   
254 component changed by 10 nT in one minute, the expected inductive electric fields (westward)  
255 could be of the order of 1.0 mV/m when shrinkage was confined within 1  $R_E$  from the  
256 equatorial plane. The dawn-dusk expansion of the flux tubes may also produce inductive  
257 electric fields (earthward and tailward in dawn and dusk sector, respectively) of the same  
258 order of magnitudes. **They are Alfvén waves, a wave mode in Ballooning instability**  
259 **coupled with slow magnetoacoustic wave [Rubtsov et al., 2018].** The westward electric  
260 fields produce earthward flow bursts referred to as convection surge. The inductive electric  
261 fields produced by the dipolarization are the same order of magnitudes observed in DF  
262 [Runov et al., 2011].

263

264

## 265 **6. Coupling of magnetosphere and ionosphere in association with field line** 266 **dipolarization**

267 The inductive electric fields may be transmitted along the field lines as poloidally and  
268 toroidally polarized Alfvén waves [Klimushkin et al., 2004]. These electric fields produce a

269 dynamic ionosphere in polar region that includes nonlinear evolution of ionospheric plasmas  
 270 (poleward expansion), as well as production of field-aligned currents and parallel potentials  
 271 by exciting ion acoustic wave in quasi-neutral condition [Saka, 2019]. It is not the aim of this  
 272 paper to describe in detail the dynamic processes in the ionosphere, but to show a local  
 273 production of currents in the ionosphere as well as field-aligned currents by the penetrated  
 274 electric fields. For this purpose, we revisit the 10 August 1994 substorm event studied by  
 275 Saka and Hayashi (2017). In this event, eastward expansion was observed of the field line  
 276 dipolarization region, started at 11:55 UT (00:27 MLT) from 260° E of geomagnetic longitudes  
 277 and expanded to 351° E in about 48 min. At the leading edge of the expansion, ground  
 278 magnetometer data showed bipolar event (quick change of the D component from positive  
 279 to negative in about 5 min), being confined in the expanding dipolarization front as a  
 280 substructure. The substructure in the leading edge of the field line dipolarization will be  
 281 examined as follows.

282 We can assume that magnetic signals on the ground are associated with the sum of the  
 283 horizontal Hall currents in the ionosphere [Fukushima, 1971]. These currents can be  
 284 calculated by the relation,

$$285 \quad (\text{rot } \mathbf{J})_z = -\frac{1}{\mu_0} \nabla^2 B_z \quad (5)$$

286 We used the ground vertical component ( $b$ ) as a proxy of  $B_z$  in the ionosphere. The second  
 287 derivative in right-hand side of equation (5) is approximated as,

$$288 \quad \nabla^2 B_z^i = \left( \frac{b^{i+1} - b^i}{L_{i+1} - L_i} - \frac{b^i - b^{i-1}}{L_i - L_{i-1}} \right) / (L_{i+1} - L_{i-1}) \quad (6)$$

289 Here,  $i$  denotes  $i$ -th station in the meridian chain.  $L_i$  is the geomagnetic latitude of the  $i$ -th  
 290 station. We considered meridional change only. This is because the vertical component  
 291 changed from negative to positive across the meridian, while in longitudes it changed simply  
 292 decreasing or increasing in lower and higher latitudes after onset, respectively. Hence,  
 293 longitudinal variations may contribute less to the Laplacian. The results reproduced from  
 294 Saka and Hayashi (2017) are shown in Figure 7(A). The eastward propagation of  
 295 dipolarization front crossed this meridian (300° E) at 12:13 UT corresponding to the interval  
 296 labelled 1. Two points arose from this figure; (1) Loop of Hall current pair existed, CCW  
 297 viewed from above the ionosphere in the lower latitudes and CW in the higher latitudes, (2)  
 298 These current patterns expand poleward. Current patterns in the interval from 1 to 5 in Figure  
 299 7(A) are illustrated in Figure 7(B) to facilitate the poleward expansion. It is clearly  
 300 demonstrated that current pair forming CW in higher latitudes and CCW in lower latitudes  
 301 expanded in time towards the pole. Bipolar change can be recorded in the D component data

302 (not shown) when the ground station, FSIM in this case, passes from segment 1 to 2 in Figure  
 303 7(B). As a result, dipolarization front expanded eastward progressively by producing the  
 304 poleward expansion at each meridian. The front left behind the current pattern comprising  
 305 upward field-aligned currents in lower latitudes and downward in higher latitudes, or Bostrom  
 306 type current system. We propose that the ionosphere itself has inherent electromotive force  
 307 to drive this Bostrom type current system. The reasons are as follows.

308 In the E region, drift trajectories may be written [Kelley, 1989] for electrons by,

$$309 \quad \mathbf{U}_{e\perp} = \frac{1}{B}[\mathbf{E} \times \hat{\mathbf{B}}] \quad (7)$$

310 and for ions by,

$$311 \quad \mathbf{U}_{i\perp} = b_i[\mathbf{E} + \kappa_i \mathbf{E} \times \hat{\mathbf{B}}]. \quad (8)$$

312 Here,  $b_i$  is mobility of ions defined as  $\Omega_i/(B\nu_{in})$ ,  $\kappa_i$  is defined as  $\Omega_i/\nu_{in}$ . Symbols  $\Omega_i$

313 and  $\nu_{in}$  are ion gyrofrequency and ion-neutral collision frequency, respectively.  $\hat{\mathbf{B}}$  denotes

314 a unit vector of the magnetic fields  $\mathbf{B}$ . We assumed that  $\mathbf{E} \times \mathbf{B}$  drifts for electrons and  
 315 ions were driven by westward electric fields transmitted from the convection surge. Because

316 of very low mobility of ions in E layer ( $\kappa_i = 0.1$ ), electric field drifts accumulate electrons (not

317 ions) in lower latitudes and produce stronger secondary southward electric fields in the

318 ionosphere. The southward electric fields produced southward motion of ions due to the first

319 term of equation (8). They carry Pedersen currents (ion currents) for producing quasi-

320 neutrality of ionosphere.  $\mathbf{E}_w \times \mathbf{B}$  drifts caused by the transmitted westward electric fields

321 ( $\mathbf{E}_w$ ) may propel electrons against southward electric fields from higher latitudes to lower

322 latitudes as electromotive force to maintain the potential drop for driving Pedersen currents.

323 This means the ionospheric E layer contains both generator and load in it. In quasi-neutral

324 condition, a small imbalance of particle densities of electrons and ions ( $n_e - n_i \sim 10^2 m^{-3}$ )

325 may induce in lower latitudes negative potential region of the order of -100 kV with horizontal

326 scale length of 100 km. To sustain this negative potential, upward field-aligned currents of

327 the order of  $1.0 \mu A / m^2$  for  $\Sigma_p \sim 10^0 S$  must flow. Downward field-aligned currents from

328 the positive potential regions in the higher latitudes may also be expected. **It is supposed**

329 that upward field-aligned currents may be carried mostly by ions flowing outwards  
330 and downward currents are escaping electrons to the magnetosphere. Those ions and  
331 electrons escape from the ionosphere into the magnetosphere to assure quasi-neutral  
332 conditions of the ionosphere. The above scenario may be adapted to a creation of the  
333 incomplete Cowling channel [Baumjohann, 1983], where unbalanced primary  
334 northward Hall currents and secondary southward Pedersen currents driven by the  
335 polarization electric fields yielded field-aligned currents.

336

337

### 338 7. Triggering mechanisms of low latitude Pi2s

339 From ground magnetometer observations in auroral zone, it is natural to assume that  
340 flux tubes linked to negative bay (decreasing of the H component) and positive bay  
341 (increasing of the H component) at higher and lower latitudes, respectively, oscillated  
342 coherently at Pi2 periods. Oscillating flux tubes associated with positive bay may  
343 produce local compression of magnetic fields in the equator and trigger cavity mode  
344 in low latitudes [Takahashi et al., 1995]. Oscillations, however, are short-lived and may  
345 not establish true cavity modes. They excite cavity/waveguide modes in the  
346 plasmasphere [Allan et al., 1996; Li et al., 1998].

347 In the dip-equator, a singular latitude of the cavity/waveguide mode, only isotropic  
348 mode can be excited [Allan et al., 1996]. This leads us to suppose that a very large  
349 propagation velocity (or large wavelength exceeding whole circle of the Earth) of  
350 equatorial Pi2s in the nightside sector [Kitamura et al., 1988] would be associated with  
351 the dawn-dusk asymmetries of non-propagating compressions.

352 Pi2 periodicity may be determined primary by consecutive arrival of BBF  
353 substructures referred to as dipolarization front bundle (DFB) [Liu et al., 2013, 2014].  
354 Repeating arrival of DFB produces periodic dipolarization or oscillation of negative  
355 bays. Positive bay oscillations in the plasmasphere would follow the negative bay  
356 oscillations to excite cavity/waveguide modes for low to equatorial Pi2s at the same  
357 periodicities. To estimate the onset time of the field line dipolarization using the very  
358 low latitudes Pi2s, delays in transmission are from the magnetosphere; longitudinal  
359 delays across the meridian may not be significant.

360 High latitude Pi2s may not be caused by cavity/waveguide modes but by oscillation of  
361 field-aligned currents comprising Bostrom type current system (incomplete Cowling  
362 channel), R1 (region 1) type current system associated with convection surge [i.e.,  
363 Birn and Hesse, 1996], and R2 (region 2) type current system of expanding flux tubes  
364 in longitudes [i.e., Tanaka et al., 2010]. In contrast to the very-low latitude Pi2s



365 associated with the non-propagating compression, the high-latitude Pi2s propagated  
366 on the ground typically at 20km/s eastward and westward in the sector east and west  
367 of the substorm center, respectively [Samson and Harrold, 1985]. Propagation across  
368 the meridian may cause further delays, 35 sec for propagation of 1 hour of local time.  
369 We should exercise caution when using high latitude Pi2s for timing study.  
370 The above scenario assumes that the DFBs arrived periodically in the inner  
371 magnetosphere at a frequency not very different than the cavity frequency of  
372 plasmasphere.

373  
374

## 375 **8. Discussion and Summary**

376 Definition of field line dipolarization is a configuration change from stretching to shrinkage of  
377 geomagnetic field lines in the midnight meridian of magnetosphere. Two models have been  
378 proposed to account for the configuration change; diversion of the cross-tail currents via  
379 ionosphere, referred to as substorm current wedge (SCW), as first proposed in McPherron  
380 et al. [1973] and extinction of the cross-tail currents by a local kinetic instability, current  
381 disruption (CD) [Lui, 1996]. These models have been adopted for many decades to account  
382 for the critical issues associated with substorm onset. We propose, based on Ballooning  
383 instability scenario, that field line dipolarization is caused by the relaxation of radial  
384 inhomogeneity of plasma pressures in association with the excitation of slow  
385 magnetoacoustic wave. Dipolarization regions expand in longitudes and decrease field  
386 magnitudes by expanding flux tubes therein. This condition continued for about 10 min and  
387 classical dipolarization caused by the reduction of cross-tail currents or pileup of the magnetic  
388 flux transported from the tail begins.

389 The proposed scenario was deduced from the geosynchronous observation and cannot be  
390 readily applied to the onset scenario beyond the geosynchronous orbit. Nevertheless, dawn-  
391 dusk expansion of the flux tubes may be a fundamental property of field line dipolarization  
392 not only at geosynchronous altitudes but also in tailward locations (8 - 12 Re) [Yao et al.,  
393 3013; Liu et al., 2013]. It is suggested that the field line dipolarization at tailward locations is  
394 subdivided by faster expanding (in longitudes) dipolarization front (DF) and slower expanding  
395 dipolarization front bundle (DFB) led by DF [Liu et al., 2015]. Such substructures in field line  
396 dipolarization are also observed at geosynchronous altitudes [Saka and Hayashi, 2017]. The  
397 geosynchronous dipolarization expanded (in longitudes) at 1.9 km/s, while Pi2s emitted in  
398 the dipolarization region propagated one order of magnitude faster. The fast longitudinal  
399 velocities associated with Pi2s may be embedded within the slowly expanding region of  
400 dipolarization, similarly to the relationship between DF and DFB. If this relationship can be

401 adapted also to the transitional state and succeeding field line pileup, the dipolarization  
402 scenario at geosynchronous observations can be extended further tailward in upstream. Or,  
403 the onset scenario in 10 Re can be applied in geosynchronous dipolarization. In that case,  
404 dipolarization pulse at Goes6 latitudes ( $7.9^\circ N$ ) may represents DFs. **This assumption**  
405 **may be supported because electron energy flux pitch angle distributions in tailward**  
406 **locations beyond 10Re show parallel to perpendicular transitions, like ones in Figure**  
407 **3, at the arrival of DF [Deng et al., 2010].**

408 We emphasize that two different types of the dipolarization exist in the substorms; one is  
409 associated with change of curvature radius of field lines in the transitional state (faster  
410 expansion in longitudes) and the other is subsequent pileup of the magnetic flux transported  
411 from the tail (slower expansion). Tailward regression of the dipolarization region as reported  
412 in Baumjohann et al. [1999] may be associated with the latter case.

413 In the transitional state lasting for about 10 min, the inductive electric fields pointing westward  
414 were produced in the equatorial plane. They propagated along the field lines to the  
415 ionosphere to produce meridional field-aligned currents of the Bostrom type (downward in  
416 higher latitudes and upward in lower latitudes). The Bostrom type current system was indeed  
417 observed on the ground at the front of dipolarization expanding towards east. The  
418 magnetospheric dynamo produced by earthward electric fields in the equatorial plane  
419 [Akasofu, 2003] and the E layer dynamo in the ionosphere worked together to activate the  
420 Bostrom current system.

421  
422

## 423 **8. Code/Data availability**

424 No data sets were used in this article.

425

## 426 **9. Competing interest**

427 The author declares that there is no conflict of interest.

428

429

## 430 Acknowledgements

431 The author would like to express his sincere thanks to all the members of Global Aurora  
432 Dynamics Campaign (GADC) [Oguti et al., 1988].

433

434

## 435 **Appendix**

436 **In order to derive equations (3) and (4), we first follow Kadomtsev (1976). Linearized**

437 MHD equations may be written as,

$$438 \quad \frac{\partial^2 \xi}{\partial t^2} = C_s^2 \nabla \operatorname{div} \xi + C_A^2 \nabla_{\perp} \operatorname{div} \xi_{\perp} + C_A^2 \frac{\partial^2 \xi_{\perp}}{\partial z^2}. \quad (\text{A1})$$

439 Here,  $C_s$ ,  $C_A$ ,  $\xi$  denote sound velocity, Alfvén velocity, plasma displacement,  
440 respectively.  $(\perp, z)$  denote perpendicular and parallel component with respect to the  
441 background field lines.

442 After a few manipulations of (A1), we have magnetoacoustic wave equations for finite  
443  $\beta$  plasmas:

$$444 \quad \frac{\partial^2 \operatorname{div} \xi_{\perp}}{\partial t^2} = C_A^2 \Delta \operatorname{div} \xi_{\perp} + C_s^2 \Delta_{\perp} \operatorname{div} \xi \quad (\text{A2})$$

445 and

$$446 \quad \frac{\partial^2 \xi_z}{\partial t^2} = C_s^2 \frac{\partial}{\partial z} (\operatorname{div} \xi) \quad (\text{A3})$$

447 Equations (A2) and (A3) present compressive properties across and along the  
448 background field lines, respectively.

449 Assuming plane harmonic wave solutions, first order quantities of density and  
450 magnetic field compressions  $(\delta n, \delta \mathbf{B})$  may be given by the following equation.

$$451 \quad \frac{\delta n}{n_0} = -\frac{C_A^2}{B_0^2} \frac{1}{C_s^2 - \left(\frac{\omega}{k}\right)^2} (\mathbf{B}_0 \cdot \delta \mathbf{B}) \quad (\text{A4})$$

452 Here,  $n_0$ ,  $B_0$  denote background density and magnetic fields, respectively.

453 Substitution of (A4) into (A3) using  $\operatorname{div} \xi = -\delta n/n_0$  yields

$$454 \quad \frac{\partial^2 \xi_z}{\partial t^2} = C_s^2 F \frac{\partial}{\partial z} (\mathbf{B}_0 \cdot \delta \mathbf{B}). \quad (\text{A5})$$

$$455 \quad \text{Here, } F = \frac{C_A^2}{B_0^2} \frac{1}{C_s^2 - \left(\frac{\omega}{k}\right)^2}$$

456 Linearized Faraday's law in frozen-in condition,  $\delta \mathbf{B} = \nabla \times (\xi_{\perp} \times \mathbf{B}_0)$ , may be reduced to

$$457 \quad \delta \mathbf{B} = -\mathbf{B}_0 \operatorname{div} \xi_{\perp} + B_0 \frac{\partial}{\partial z} \xi_{\perp}. \quad (\text{A6})$$

458 Substituting (A6) into (A5), we have final expressions relating parallel and  
459 perpendicular displacements as,

$$460 \quad \frac{\partial^2 \xi_z}{\partial t^2} = -C_s^2 F \cdot B_0^2 \frac{\partial}{\partial z} (\operatorname{div} \xi_{\perp}). \quad (\text{A6})$$

461 **Replacing  $\partial/\partial t$  with  $-i\omega$ , (A6) yields the equation (3) in Section 4,**

462 
$$\xi_z = \frac{C_S^2}{\omega^2} F \cdot B_0^2 \frac{\partial}{\partial z} (\text{div} \xi_{\perp}).$$

463

464

465

466 **References**

467 Akasofu, S.-I.: Source of auroral electrons and the magnetospheric substorm current system,  
468 J. Geophys. Res., 108, A4, 8006, doi:10.1029/2002JA009547, 2003.

469 Allan, W., F.W. Menk, B.J. Fraser, Y. Li, and S.P. White, Are low-latitude Pi2 pulsations  
470 cavity/waveguide mode?, Geophys. Res. Lett., 23, 765, 1996.

471 Baumjohann, W.: Ionospheric and field-aligned current systems in the auroral zone: A  
472 concise review, Adv. Space Res., 2, 55-62, 1983.

473 Baumjohann, W., Hesse, M., Kokubun, S., Mukai, T., Nagai, T., and Petrukovich, A.A.:  
474 Substorm dipolarization and recovery, J. Geophys. Res., 104, 24995-25000, 1999.

475 Birn, J., and Hesse, M.: Details of current disruption and diversion in simulations of  
476 magnetotail dynamics, J. Geophys. Res., 101, A7, 15345-15358, 1996.

477 Birn, J., Thomsen, M.F., Borovsky, J.E., Reeves, G.D., McComas, D.J., and Belian, R.D.:  
478 Characteristic plasma properties during dispersionless substorm injections at  
479 geosynchronous orbit, J. Geophys. Res., 102, A2, 2309-2324, 1997.

480 Deng, X, Ashour-Abdalla, M., Zhou, M., Walker, R., El-Alaoui, M., Angelopoulos, V., Ergun,  
481 R.E., and Schriver, D.: Wave and particle characteristics of earthward electron  
482 injections associated with dipolarization fronts, J. Geophys. Res., 115, A09225,  
483 doi:10.1029/2009JA015107, 2010.

484 Fairfield, D.H., Mukai, T., Brittnacher, M., Reeves, G.D., Kokubun, S., Parks, G.K., Nagai, T.,  
485 Mtsumoto, H., Hashimoto, K., Gurnett, D.A., and Yamamoto, T.: Earthward flow bursts  
486 in the inner magnetotail and their relation to auroral brightenings, AKR intensifications,  
487 geosynchronous particle injections and magnetic activity, J. Geophys. Res., 104, A1,  
488 355-370, 1999.

489 Fukushima, N.: Electric current systems for polar substorms and their magnetic effect below  
490 and above the ionosphere, Radio Sciences, 6, 269-275, 1971.

491 Kadomtsev, B.B.: Collective phenomena in plasmas (in Japanese), Iwanami shoten, Tokyo,  
492 1976.

493 Kelley, M.C.: The earth's ionosphere: plasma physics and electrodynamics, Academic Press,  
494 Inc, 1989.

495 Kitamura, T., Saka, O., Shimoizumu, M., Tachihara, H., Oguti, T., Araki, T., Sato, N., Ishitsuka,  
496 M., Veliz, O., and Nyobe, J.B.: Global mode of Pi2 waves in the equatorial region:  
497 Difference of Pi2 mode between high and equatorial latitudes, *J. Geomag. Geoelectr.*,  
498 40, 621-634, 1988.

499 Klimushkin, D.Yu., Mager, P.N., and Glassmeier, K.-H.: Toroidal and Poloidal Alfvén waves  
500 with arbitrary azimuthal wave numbers in a finite pressure plasma in the Earth's  
501 magnetosphere, *Annales Geophysicae*, 22, 267-287, 2004.

502 Li, Y., B.J. Fraser, F.W. Menk, D.J. Webster, and K. Yumoto, Properties and sources of low  
503 and very low latitude Pi2 pulsations, *J. Geophys. Res.*, 103, 2343, 1998.

504 Liu, J., Angelopoulos, V., Runov, A., and Zhou, X.-Z.: On the current sheets surrounding  
505 dipolarizing flux bundles in the magnetotail: The case for wedgelets, *J. Geophys. Res.*,  
506 118, 2000-20120, doi:10.1002/jgra50092, 2013.

507 Liu, J., Angelopoulos, V., Zhou, X.-Z., and Runov, A.: Magnetic flux transport by dipolarizing  
508 flux bundles, *J. Geophys. Res.*, 119, 909-926, doi:10.1002/2013JA019395, 2014.

509 Liu, J., Angelopoulos, V., Zhou, X.-Z., Yao, Z.-H., and Runov, A.: Cross-tail expansion of  
510 dipolarizing flux bundles, *J. Geophys. Res.*, 120, 2516-2530,  
511 doi:10.1002/2015JA020997, 2015.

512 Lui, A.T.Y.: Current disruption in the Earth's magnetosphere: Observations and models, *J.*  
513 *Geophys. Res.*, 101, 13067-13088, 1996.

514 Machida, S., Miyashita, Y., Ieda, A., Nose, M., Nagata, D., Liou, K., Obara, T., Nishida, A.,  
515 Saito, Y., and Mukai, T.: Statistical visualization of the Earth's magnetotail based on  
516 Geotail data and the implied substorm model, *Ann. Geophys.*, 27, 1035-1046, 2009.

517 Machida, S., Miyashita, Y., Ieda, A., Nose, M., Angelopoulos, V., and McFadden, J.P.:  
518 Statistical visualization of the Earth's magnetotail and the implied mechanism of  
519 substorm triggering based on superposed-epoch analysis of THEMIS data, *Ann.*  
520 *Geophys.*, 32, 99-111, 2014.

521 McPherron, R.L., Russell, C.T., and Aubry, M.P.: Satellite studies of magnetospheric  
522 substorms on August 15, 1968: 9. Phenomenological model for substorms, *J.*  
523 *Geophys. Res.*, 78, 3131-3148, 1973.

524 Miyashita, Y., Machida, S., Kamide, Y., Nagata, D., Liou, K., Fujimoto, M., Ieda, A., Saito,  
525 M.H., Russell, C.T., Christon, S.P., Nose, M., Frey, H.U., Shinohara, I., Muaki, T., Saito,  
526 Y., and Hayakawa, H.: A state-of-the-art picture of substorm-associated evolution of  
527 the near-Earth magnetotail obtained from superposed epoch analysis, *J. Geophys.*  
528 *Res.*, 114, A01211, doi:10.1029/2008JA013225, 2009.

529 Morioka, A., Miyoshi, Y., Miyashita, Kasaba, Y., Misawa, H., Tsuchiya, F., Kataoka, R.,  
530 Kadokura, A., Mukai, T., Yumoto, K., Menietti, D.J., Parks, G., Liou, K., Honary, and

531 Donovan, E.: Two-step evolution of auroral acceleration at substorm onset, *J.*  
532 *Geophys. Res.*, 115, A11213, doi:10.1029/2010JA015361, 2010.

533 Nagai, T., Fujimoto, M., Saito, Y., Machida, S., Terasawa, T., Nakamura, R., Yamamoto, T.,  
534 Mukai, T., Nishida, A., and Kokubun, S.: Structure and dynamics of magnetic  
535 reconnection for substorm onsets with Geotail observations, *J. Geophys. Res.*, 103,  
536 A3, 4419-4440, 1998.

537 Nakamura, R., Baumjohann, W., Brittnacher, M., Sergeev, V.A., Kubyshkina, Mukai, T., and  
538 Liou, K.: Flow bursts and auroral activations: Onset timing and foot point location, *J.*  
539 *Geophys. Res.*, 106, A6, 10777-10789, 2001.

540 Oguti, T., Kitamura, T., and Watanabe, T.: Global aurora dynamics campaign, 1985-1986, *J.*  
541 *Geomag. Geoelectr.*, 40, 485-504, 1988.

542 Ohtani, S.-I., Miura, A., and Tamao, T.: Coupling between Alfvén and slow magnetosonic  
543 waves in an inhomogeneous finite- $\beta$  plasma: 1 Coupled equations and physical  
544 mechanism, *Planet. Space Sci.*, 37, 567-577, 1989.

545 Ohtani, S.-I., and Tamao, T.: Does the ballooning instability trigger substorms in the near-  
546 earth magnetotail?, *J. Geophys. Res.*, 98, A11, 19369-19379, 1993.

547 Ohtani, S.-I., Motoba, T., Gkioulidou, M., Takahashi, K., and Singer, H.J.: Spatial development  
548 of the dipolarization region in the inner magnetosphere, *J. Geophys. Res.*, 123, 5452-  
549 5463, doi.org/10.1029/2018JA025443.

550 Rubtsov, A.V., Mager, P.N., and Klimushkin, D.Yu.: Ballooning instability of azimuthally small  
551 scale coupled Alfvén and slow magnetoacoustic modes in two-dimensionally  
552 inhomogeneous magnetospheric plasma, *Physics of Plasmas* 25, 102903,  
553 doi:10.1063/1.5051474, 2018.

554 Runov, A., Angelopoulos, V., Zhou, X.-Z., Zhang, X.-J., Li, S., Plaschke, F., and Bonnell, J.:  
555 A THEMIS multicasestudy of dipolarization fronts in the magnetotail plasma sheet,  
556 116, A05216, doi:10.1029/2010JA016316, 2011.

557 Saka, O., Akaki, H., and Baker, D.N.: A satellite magnetometer observation of dusk-to-dawn  
558 current in the midnight magnetosphere at low-latitude Pi2 onset, *Earth Planets Space*,  
559 54, e1-e4, 2002

560 Saka, O., Hayashi, K., and Thomsen, M.: First 10 min intervals of Pi2 onset at  
561 geosynchronous altitudes during the expansion of energetic ion regions in the  
562 nighttime sector, *J. Atmos. Solar Terr. Phys.*, 72, 1100-1109, 2010.

563 Saka, O., Hayashi, K., and Koga, D.: Excitation of the third harmonic mode in meridian planes  
564 for Pi2 in the auroral zone, *J. Geophys. Res.*, 117, A12215,  
565 doi:10.1029/2012JA018003, 2012.

566 Saka, O., and Hayashi, K.: Longitudinal expansion of field line dipolarization, *J. Atmos. Solar*

567 Terr. Phys., 164, 235-242, 2017.

568 Saka, O.: A new scenario applying traffic flow analogy to poleward expansion of auroras, Ann.  
569 Geophys., 37, 381-387, 2019.

570 Sakurai, T., and Saito, T.: Magnetic pulsation Pi2 and substorm onset, Planet. Space Sci., 24,  
571 573-575, 1972.

572 Samson, J.C., and B.G. Harrold, Characteristic time constant and velocities of high-latitude  
573 Pi2's, J. Geophys. Res., 90, 12173, 1985.

574 Takahashi, K., Ohtani, S.-I., and Anderson, B.J.: Statistical analysis of Pi2 pulsations  
575 observed by the AMPTE CCE spacecraft in the inner magnetosphere, J.Geophys.Res.,  
576 100, A11, 21929-21941, 1995.

577 Takahashi, K., Anderson, B.J., and Ohtani, S.-I.: Multisatellite study of nightside transient  
578 toroidal waves, J.Geophys.Res., 101, A11, 24815-24825, 1996.

579 Tanaka, T., Nakamizo, A., Yoshikawa, A., Fujita, S., Shinagawa, H., Shimazu, H., Kikuchi, T.,  
580 and Hashimoto, K.K.: Substorm convection and current system deduced from the  
581 global simulation, J.Geophys.Res. 115, A05220, doi:10.1029/2009JA014676, 2010.

582 Yao, Z, Sun, W.J., Fu, S.Y., Pu, Z.Y., Liu, J., Angelopoulos, V., Zhang, X.-J., Chu, X.N., Shi,  
583 Q.Q., Guo, R.L., and Zong, Q.-G.: Current structures associated with dipolarization  
584 fronts, J.Geophys.Res., 118, 6980-6985, doi:10.1002/2013JA019290, 2013.

585

586

587

588

589

590

591

592

593

594

595

596

597

598

599

600

601

602

603 Figure captions

604

605 **Figure 1.**

606 **Upper panel: Local time distribution of W event and E event (see below). Lower panels:**  
607 **Epoch superposition of field line deflections in degrees for Goes5/6. Those events**  
608 **with eastward deflections (clockwise rotation, azimuth angle decreased) at T=0 shown**  
609 **to the left (E event) and those with westward deflections (counterclockwise rotation,**  
610 **azimuth angle increase) at T=0 are to the right (W event). T=0 marked by vertical dotted**  
611 **lines corresponds to the first peak of the Pi2 waveform. Amplitudes at the onset (T=0)**  
612 **were subtracted from the original data to adjust the pre-onset level. Plots covered 40**  
613 **min from T-10 min to T+30 min. Mean value of the epoch plot and mean value of band-**  
614 **passed (6-20 mHz: Pi2 band) amplitudes are also shown. The field line rotations**  
615 **projected to the equatorial plane are illustrated for E event and W event in the Figure**  
616 **(viewed from north of the equatorial plane).**

617

618

619 **Figure 2.**

620 **A progress of field line thinning in the growth phase is illustrated. The inflow flux ( $F_{\perp}$ )**  
621 **rotated counterclockwise in times designated by red, green, and to blue arrows north**  
622 **of the equatorial plane. South of the equatorial plane, rotation was in a clockwise**  
623 **direction. The rotation of the inflow vectors produced the field-aligned component of**  
624 **the flux,  $\delta F_{\parallel} = F_{\perp}(\omega \cdot \delta t)$  as depicted in the inset with one in the northern**  
625 **hemisphere shown. Note that inflows are localized earthward of the outer field lines.**

626

627

628 **Figure 3.**

629 **Simulated pitch angle spectrogram of energy flux for drift Maxwell distributions of**  
630 **phase space density. Energy flux was shown in contour plots with arbitrary amplitudes.**  
631 **To show how the pitch angle spectrogram evolves, drift velocities in parallel and**  
632 **perpendicular directions with respect to the background magnetic fields have**  
633 **changed. No drifts in both perpendicular and parallel to the background field lines (A).**  
634 **Only parallel drifts increased;  $0.3V_{th}$  (B),  $0.6V_{th}$  (C) and  $1.0V_{th}$  (D). For (E) and (F),**  
635 **perpendicular drift increased to  $0.3V_{th}$  and  $0.5V_{th}$  while parallel drift remained at  $1.0V_{th}$ .**  
636  **$V_{th}$  denotes thermal velocity. The vertical axis is for pitch angles, while the horizontal**



637 axis is for particle energies normalized by the thermal energy.

638

639

640 **Figure 4.**

641 **(A) Multiple Pi2 event (1, 2, 3, and 4 labelled in the Figure) with positive bay observed**

642 **at low latitude station (KUJ) at L=1.2 in the midnight sector (23:42 MLT at 15:00 UT).**

643 **The figure, from 1430 UT to 1600 UT 31 August 1986, was reproduced from [Saka et al.,**

644 **2002]. (B) Inclination angle of field lines in dipole coordinates along the satellite**

645 **trajectories measured by AMPTE CCE spacecraft. Inclination angle ( $\theta$ ) was defined**

646 **as  $\theta = \text{Tan}^{-1}\left(H/\sqrt{V^2 + D^2}\right)$ . H is positive northward parallel to the dipole axis, V is**

647 **radial outward, and D is dipole east. Vertical arrows denote dipolarization onset**

648 **corresponding to the multiple Pi2; 1, 2, 3, and 4 in panel A. (C) Difference of duskward**

649 **flux (counts/sample) ( $J_-$ ) and dawnward flux ( $J_+$ ) for 63-85 keV ion channel measured**

650 **by AMPTE CCE spacecraft. (D) Same as for (C) but for 125-210 keV ion channel.**

651 **Radial distance (R) in Re, MLaT in degrees, and MLT at 14:30 UT, 15:00 UT and 16:00**

652 **UT along satellite trajectory are shown in the bottom.**

653

654

655 **Figure 5.**

656 **A schematic illustration of particle measurement in X-Y plane of GSE coordinates; X**

657 **is earthward, Y is duskward in ecliptic plane. For the time interval of multiple Pi2 event**

658 **when the satellite was at 22 MLT, duskward flux represented by ( $J_-$ ) came from the**

659 **earthward sector and dawnward flux ( $J_+$ ) from tailward sector.  $J_- > J_+$  because of**

660 **the pressure gradient positive earthward. Spatial gradient represented by solid line**

661 **relaxed to dotted line. Radial separation,  $X_1 - X_2$ , is either 1000 km or 1800 km for 63-**

662 **85 keV ions or 125-210 keV ions, respectively.**

663

664

665 **Figure 6.**

666 **A schematic illustration of the field line deformations in the meridian plane associated**

667 **with the changing curvature radius of the field lines. The outer field lines marked by**

668 **(1) changed to field lines (2) by increasing their curvature radius to R1 (red-dashed**

669 **circle) in association with the relaxation of radial inhomogeneity, while the inner field**  
670 **lines marked by (3) moved to field lines (4) of smaller curvature radius R2 (blue-dashed**  
671 **circle). This transition, (3) to (4), may be caused by the radial gradient of magnetic**  
672 **pressures becoming steeper in association with the inward compression of the field**  
673 **lines (see text). In the inset, flux tube deformations in the equatorial cross section is**  
674 **illustrated at onset locations (field lines 1 and 2). Divergence of perpendicular flows in**  
675 **dawn-dusk directions (solid arrows) produced dawn-dusk expansion of flux tube (2)**  
676 **coincide with the shrinkage of stretched flux tube (1). Flux tube deformation from 1 to**  
677 **2 tended to preserve the total magnetic fluxes in the equatorial cross section.**

678

679

680 Figure 7.

681 (A) Vertical component of  $(rot \mathbf{J})_Z$  in the meridian chain along  $300^\circ E$  for the interval from  
682 1000 UT to 1500 UT, reproduced from Saka and Hayashi (2017). Dipolarization onset was  
683 at 12:13 UT at this meridian. For the calculation of  $(rot \mathbf{J})_Z$ , vertical component data from  
684 RES ( $83.0^\circ N, 299.7^\circ E$ ), CBB ( $76.6^\circ N, 301.2^\circ E$ ), CONT ( $72.6^\circ N, 298.3^\circ E$ ), YKC ( $68.9^\circ N,$   
685  $298.0^\circ E$ ), FSIM ( $67.2^\circ N, 290.8^\circ E$ ), FSJ ( $61.9^\circ N, 295.5^\circ E$ ), and VIC ( $54.1^\circ N, 296.7^\circ E$ ) along  
686 the magnetic meridian  $300^\circ E$  were used (see text). Positive for the clockwise rotation (CW)  
687 of ionospheric currents and negative for the counterclockwise rotation (CCW) viewed from  
688 above the ionosphere. Amplitudes are color-coded. The scale is shown on the right.  
689 Demarcation lines separating CCW and CW in latitudes are marked by dashed line. The  
690 demarcation line moved to poleward after the onset. Note that negative  $(rot \mathbf{J})_Z$  in  
691 poleward edge indicates smooth decrease of the Z amplitudes.

692

693 (B) Time progresses of the CW/CCW patterns are illustrated separately in five segments from  
694 1 to 5 marked in Figure 7 (A). The figure demonstrates a progress of CW/CCW pair in time,  
695 CW in the poleward and CCW in the equatorward. This pair developed its size after onset  
696 showing poleward expansion. The meridional current associated with this pair of loop current,  
697 if closed in the equatorial plane via the field-aligned currents, comprised the Bostrom type  
698 current system.

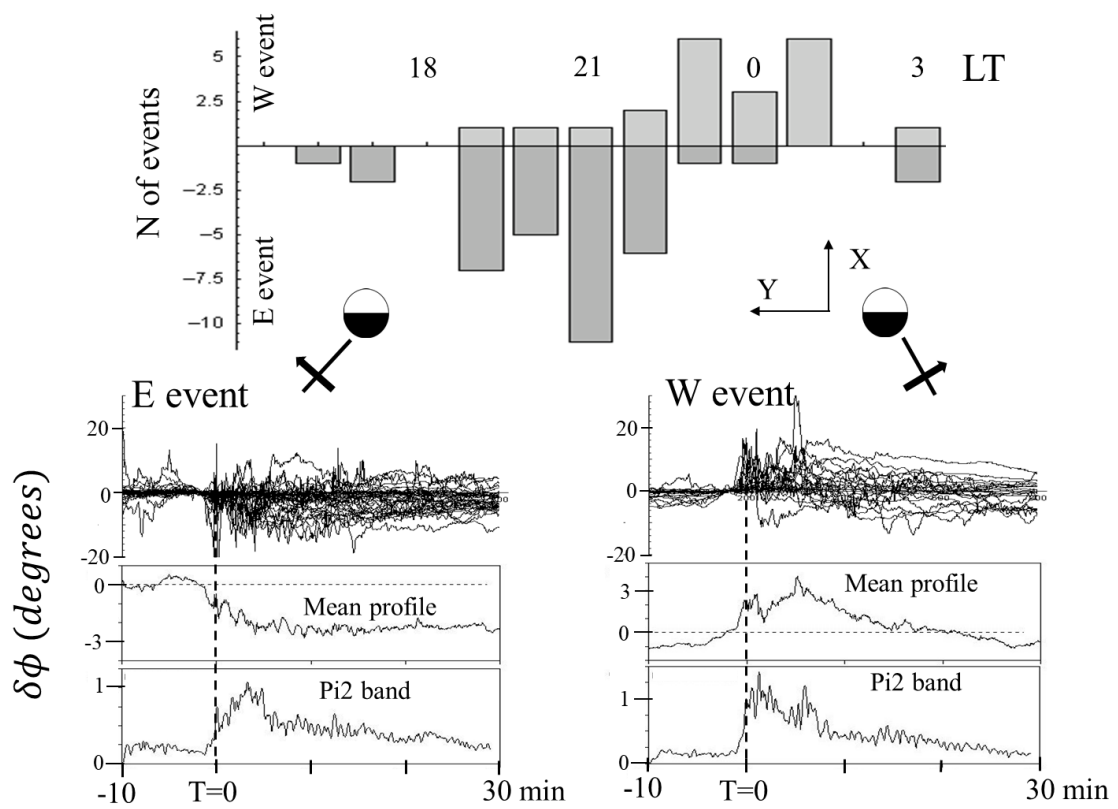


Figure 1

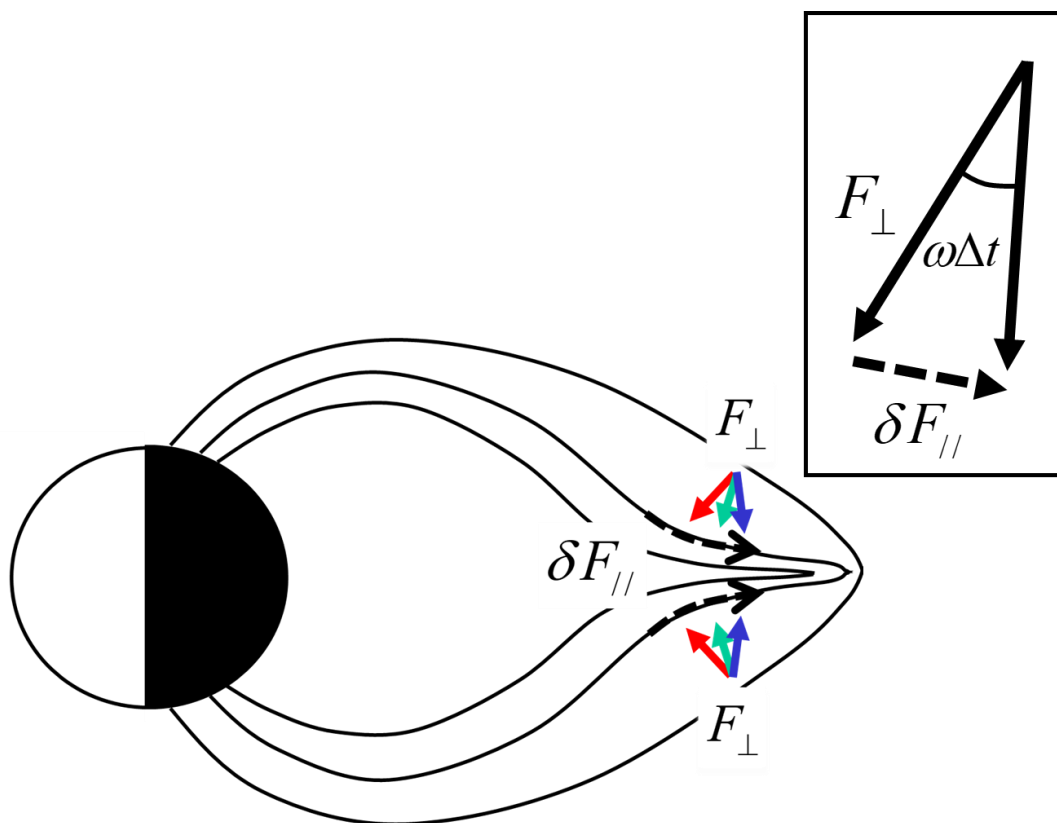


Figure 2

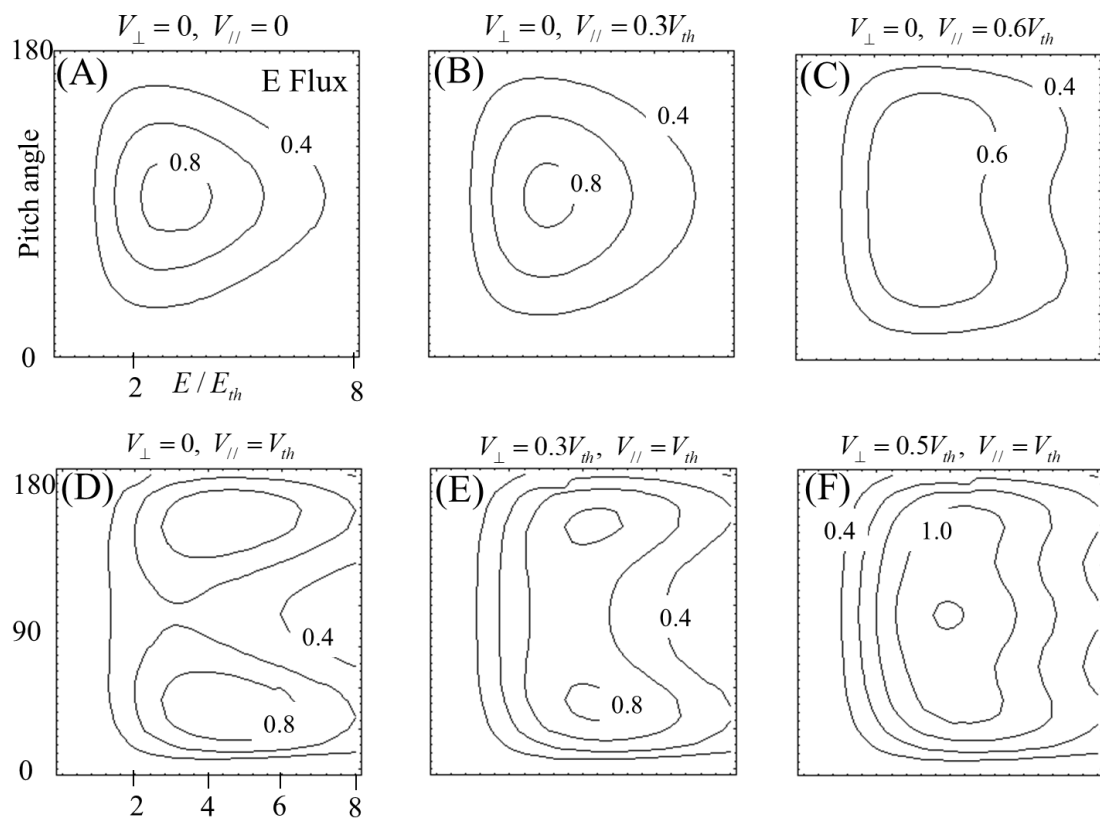


Figure 3

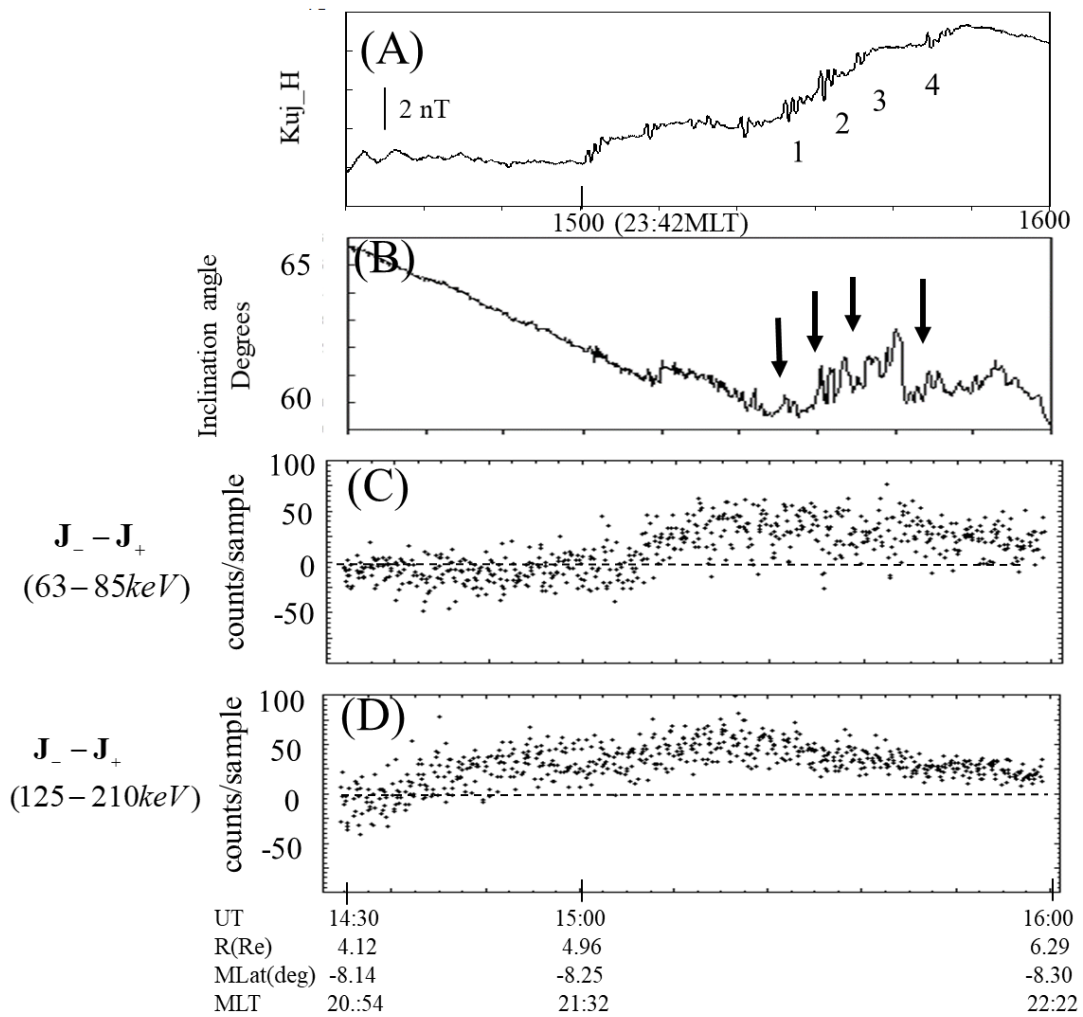


Figure 4

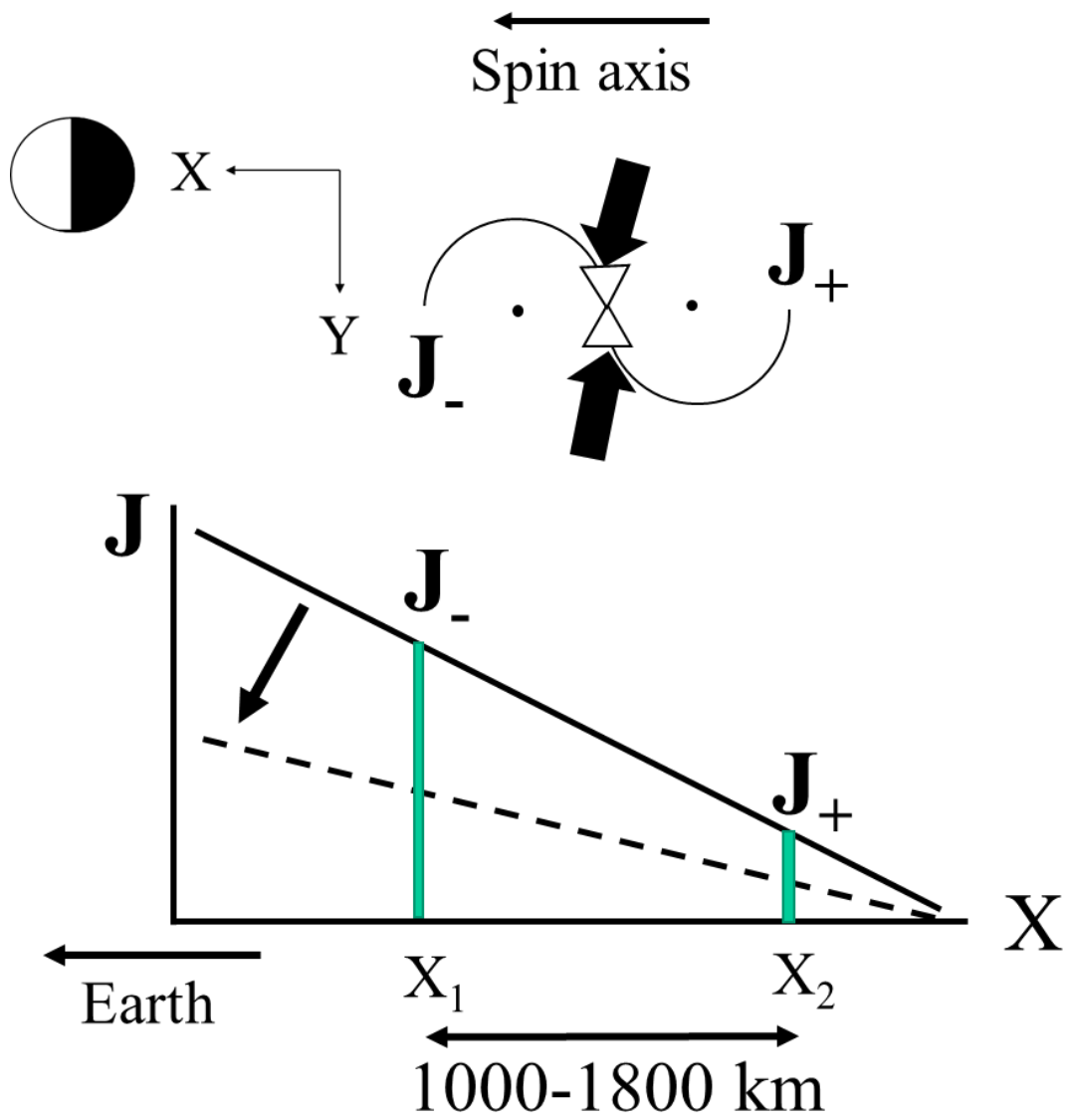


Figure 5

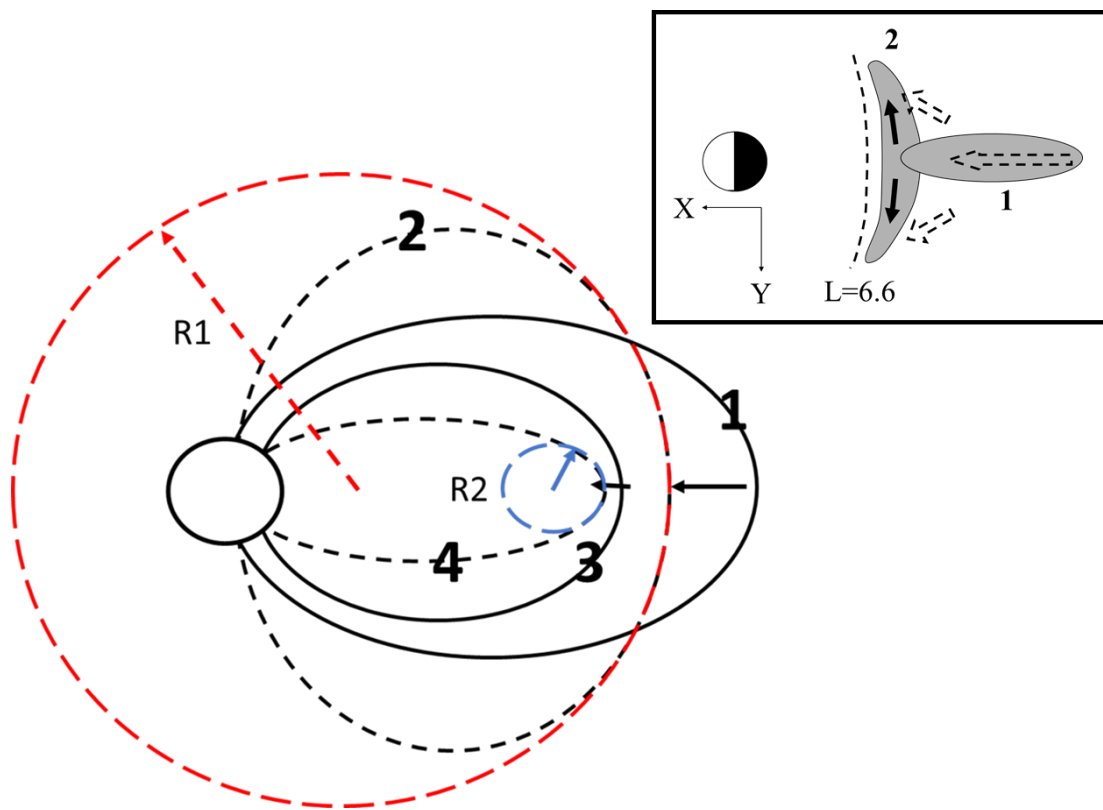


Figure 6



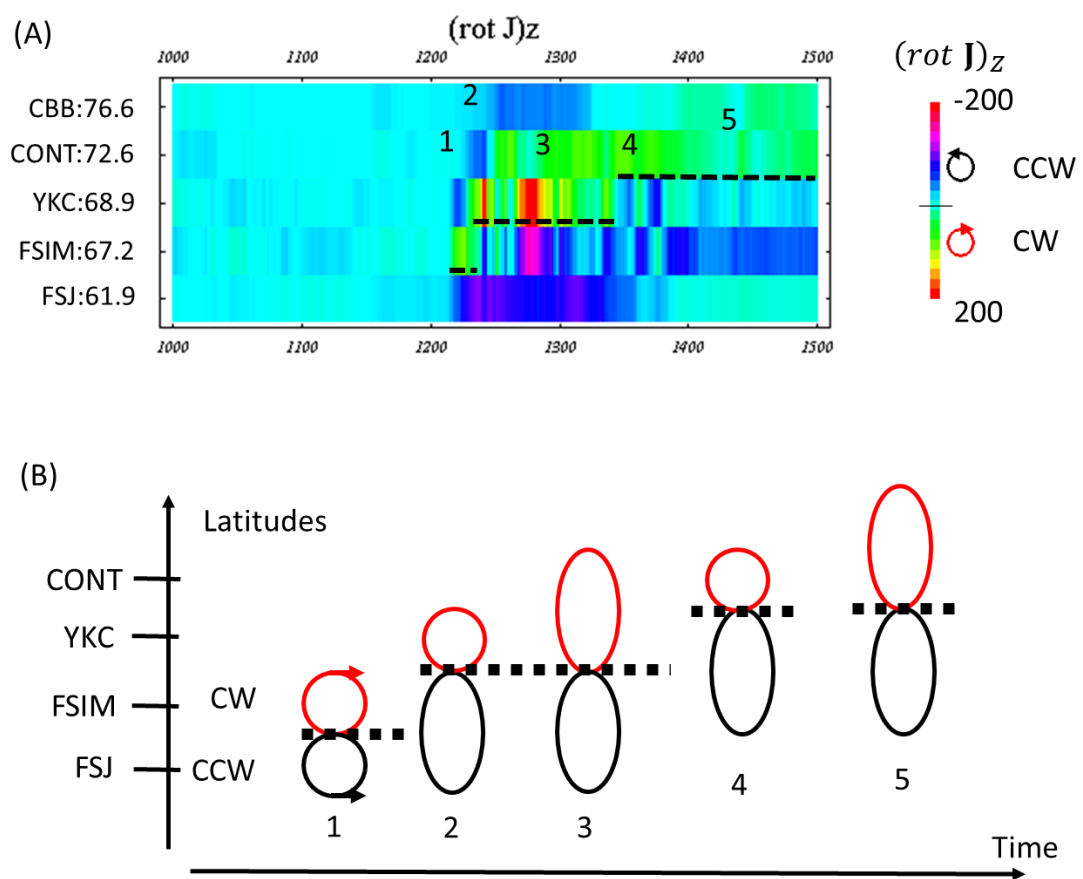


Figure 7